DNS and modeling of a turbulent boundary layer with separation and reattachment over a range of Reynolds numbers

By H. Abe, Y. Mizobuchi, Y. Matsuo AND P. R. Spalart

1. Motivation and objectives

The separation of a turbulent boundary layer, which is encountered in devices such as airfoils, diffusers and turbomachinery, is one of the most challenging research topics in fluid mechanics. Its understanding and its prediction with turbulence models are however still not satisfactory. The reason may be partly due to a shortage of reliable data from numerical simulations, which account for Reynolds number dependence systematically.

Direct numerical simulation (DNS) yields accurate and detailed turbulence quantities, thus allowing the development of turbulence models based on much more complete information than experiments provide. A large number of DNS databases have been established in canonical flows (i.e., homogeneous, channel, pipe and boundary layer) so far, where significant attention is given to Reynolds number effects. For separated flows, on the other hand, there is still limited information available from DNS due perhaps to difficulties associated with inflow, boundary conditions, domain size and ultimately computing cost. In particular, unlike for separation forced by the configuration of such a backward-facing step, only a few DNS attempts have been made for pressure-induced separation in a flat-plate turbulent boundary layer. For the latter DNS, seminal studies were carried out by Spalart & Coleman (1997) and Na & Moin (1998) at Reynolds number $Re_\theta \equiv U_\infty \theta_0/\nu = 300$ (U_∞ and θ_0 denote the freestream velocity and inlet momentum thickness, respectively, and ν is the kinematic viscosity) where the former (Spalart & Coleman 1997) and latter (Na & Moin 1998) dealt with incipient and massive separation, respectively. Later, Skote & Henningson (2002) achieved the DNS at $Re_\theta = 300$ but with a large recirculation region. Manhart & Friedrich (2002) performed the DNS at a higher Reynolds number of $Re_\theta = 870$. However, the Re dependence of the mean and turbulence quantities together with turbulence structure has yet to be examined.

Currently, we are working on a series of DNS of a turbulent boundary layer with separation and reattachment where a relatively large magnitude of blowing and suction is imposed at the upper boundary, producing a large separation bubble. The inlet Reynolds number Re_θ is equal to 300, 600 and 985, the latter value being about three times larger than that in the seminal DNS works (Spalart & Coleman 1997; Na & Moin 1998), but still only about half of that in the Simpson (1989) experiment. The objectives of the present study are to establish DNS databases at higher Reynolds numbers, then to clarify the Reynolds number dependence in turbulent separation and reattachment, and finally to develop turbulence models for RANS and LES using the DNS data. Note that the present Re range still does not overlap with that in the Song & Eaton (2004) experiment ($Re_\theta = 1100 \sim 20100$), which also focused on the Reynolds number effects in a smoothly contoured ramp; low Reynolds number effects (Purtell *et al.* 1981) cannot be dismissed when interpreting the current DNS results, but the range is quite wide.

Re_θ	300	600	985
$L_x \times L_y \times L_z$	$400\theta_0 \times 120\theta_0 \times 80\theta_0$	$400\theta_0 \times 120\theta_0 \times 160\theta_0$	$365\theta_0 \times 110\theta_0 \times 146\theta_0$
$N_x \times N_y \times N_z$	$512 \times 320 \times 256$	$1024 \times 640 \times 1024$	$2048 \times 960 \times 1536$
Δx_0^+, Δy_0^+, Δz_0^+	12.4, 0.13∼16.8, 4.95	11.4, 0.11∼15.4, 4.56	7.92, 0.11∼14.3, 4.22

TABLE 1. Domain size, grid points and spatial resolution.

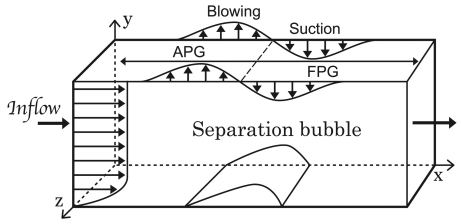

FIGURE 1. Computational domain.

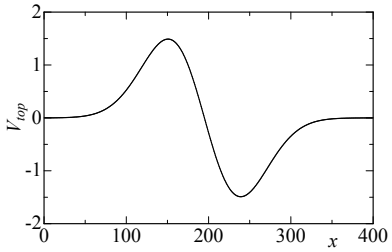

FIGURE 2. Transpiration velocity profile.

This brief is organized as follows. The numerical methodology is explained shortly in Section 2. Section 3 consists of three subsections. Shown in §3.1 are representative DNS results for $Re_\theta = 300$ with a focus on the effects of streamline curvature in a separation bubble. In §3.2, attention is given to the Reynolds number dependence on both turbulence statistics and structures in the bubble; the similarity to a mixing layer is also examined. §3.3 presents results regarding the evaluation for two-equation turbulence models (i.e., k-ε by Abe *et al.* 1994, k-ω by Wilcox 1988 and SST by Menter 1994) using the DNS data; the sensitivity of freestream disturbances is also discussed. It is hoped that, although in separated flows different performance is obtained for different geometries (see the recent review by Leschziner 2006), the present testing will provide further insight into model performance and hence be useful for developing turbulence models for separated flows.

2. Numerical methodology

The computational domain is given in Figure 1 where x, y and z are the streamwise, wall-normal and spanwise directions, respectively. Note that throughout the paper, all variables are normalized by U_∞ and θ_0 unless otherwise stated. The inflow data prescribed are DNS data in an incompressible zero-pressure-gradient turbulent boundary layer generated by the rescaling-recycling method (Lund *et al.* 1998), while a convective boundary condition is used for the outlet. Three values of Re_θ(=300, 600 and 985) are used. The corresponding Re_τ ($\equiv u_\tau \delta_{99}/\nu$) is equal to 139, 250 and 353 (u_τ and δ_{99} denote the friction velocity and 99% boundary layer thickness). The transpiration profile V_{top} given at the upper boundary is shown in Figure 2 where the magnitude of blowing and suction is about three times larger (but imposed on a higher line) than that of Spalart & Coleman (1997) as needed to have massive separation. This V_{top} profile is uniform in the z direction, thus the periodic boundary condition is used in this direction. The present study hence deals with two-dimensional separation. The boundary condition at the upper boundary is a no-vorticity boundary condition (viz. $\Omega_z(\equiv U_{2,1} - U_{1,2}) = 0$) to ensure the conservation of momentum flux, whilst a no-slip condition is used at the wall.

The numerical methodology is briefly as follows. The current DNS code has been developed based on the channel DNS code (Abe *et al.* 2004*b*). A fractional step method is used with semi-implicit time advancement. The Crank-Nicolson method is used for the viscous terms in the y direction, and the 3rd-order Runge-Kutta method is used for the other terms. A finite difference method is used as a spatial discretization. A 4th-order central scheme (Morinishi *et al.* 1998) is used in the x and z directions, whilst a 2nd-order central scheme is used in the y direction. The computational domain size ($L_x \times L_y \times L_z$), number of grid points ($N_x \times N_y \times N_z$) and spatial resolution at the inlet (Δx_0^+, Δy_0^+, Δz_0^+) are given in Table 1 where the superscripts + denotes normalization by wall units. Note that the domain size for $Re_\theta = 985$ is about 9 percent smaller than that for $Re_\theta = 300$ and 600 so that in the subsequent plots, the x location for $Re_\theta = 985$ is adjusted to have the same $V_{top} = 0$ location as for $Re_\theta = 300$ and 600.

3. Results and discussion

3.1. *Statistics and streamline curvature effects*

First, representative statistics for $Re_\theta = 300$, such as the mean streamwise velocity $\bar{U}$ and turbulent kinetic energy $k\ (\equiv \overline{u_i u_i}/2)$, its production $P_k\ (\equiv -\overline{u_i u_j} S_{ij})$ and energy dissipation rate $\varepsilon\left(\equiv \overline{u_{i,j}\left(u_{i,j}+u_{j,i}\right)}\right)$, are shown in Figure 3. Note that $S_{ij} \equiv \left(\bar{U}_{i,j} + \bar{U}_{j,i}\right)/2$; the suffixes 1,2,3 denote the streamwise, wall-normal and spanwise component, respectively; u_1, u_2, u_3 are sometimes used interchangeably with u, v, w, respectively; upper and lower cases are instantaneous and fluctuating quantities; an overbar indicates the averaging in the z direction and time. In the separation bubble, we see clear backflow in the distribution of $\bar{U}$ (Figure 3*a*), indicating massive separation. As for turbulence quantities, large magnitudes appear in the separated shear layer and reattached region (Figures 3*b*–3*d*). Their magnitudes are however attenuated at the top of the bubble. In particular, P_k displays a negative value, which is of course unusual, where the streamline curvature is at its most convex (Figure 3*d*). An indicator of streamwise curvature $\bar{U}_{2,1}$, which comes from a rapid pressure-driven change of the mean strain rate, is associated with negative P_k. That is, the budget term arising from $\bar{U}_{2,1}$ (not shown here) yields negative Reynolds shear stress ($-\overline{u_1 u_2} < 0$) (Figure 3*e*), and then the product of $-\overline{u_1 u_2}$ and $\bar{U}_{1,2}$ contributes to negative P_k. We note that these quantities are defined in the wall and wall-normal axes, which is non-unique for turbulence that is relatively far from the wall. However, there is also correspondence between regions with negative P_k and negative Reynolds shear stress if this stress is defined in the streamline orthogonal coordinate system, i.e., $\overline{ab} = \left[\left(\overline{u_2 u_2} - \overline{u_1 u_1}\right)\bar{U}_1\bar{U}_2 + \overline{u_1 u_2}\left(\bar{U}_1^2 - \bar{U}_2^2\right)\right] / \left(\bar{U}_1^2 + \bar{U}_2^2\right)$ (Figures 3*d* and *f*). Note the large difference between $\overline{u_1 u_2}$ and $\overline{ab}$ in the region $100 < x < 200$.

This figure has an intriguing pattern involving production and dissipation. Negative production centered on $x = 210$ is followed by a large drop in dissipation centered on $x = 245$. This may seem natural, but is not very in line with turbulence theory. Theory would predict that negative production is first reflected in a reduced turbulent kinetic energy, and later by a reduced dissipation, after the energy cascade reaches the small scales. This is because strain directly affects the anisotropic large scales. Here, a very mild drop in k is visible in Figure 3(b) (visibility is further hampered by the lack of color in the contours) which is puzzling. It will be most interesting to study the same pattern at higher Reynolds numbers, when the scale separation and the energy cascade are much more in place.

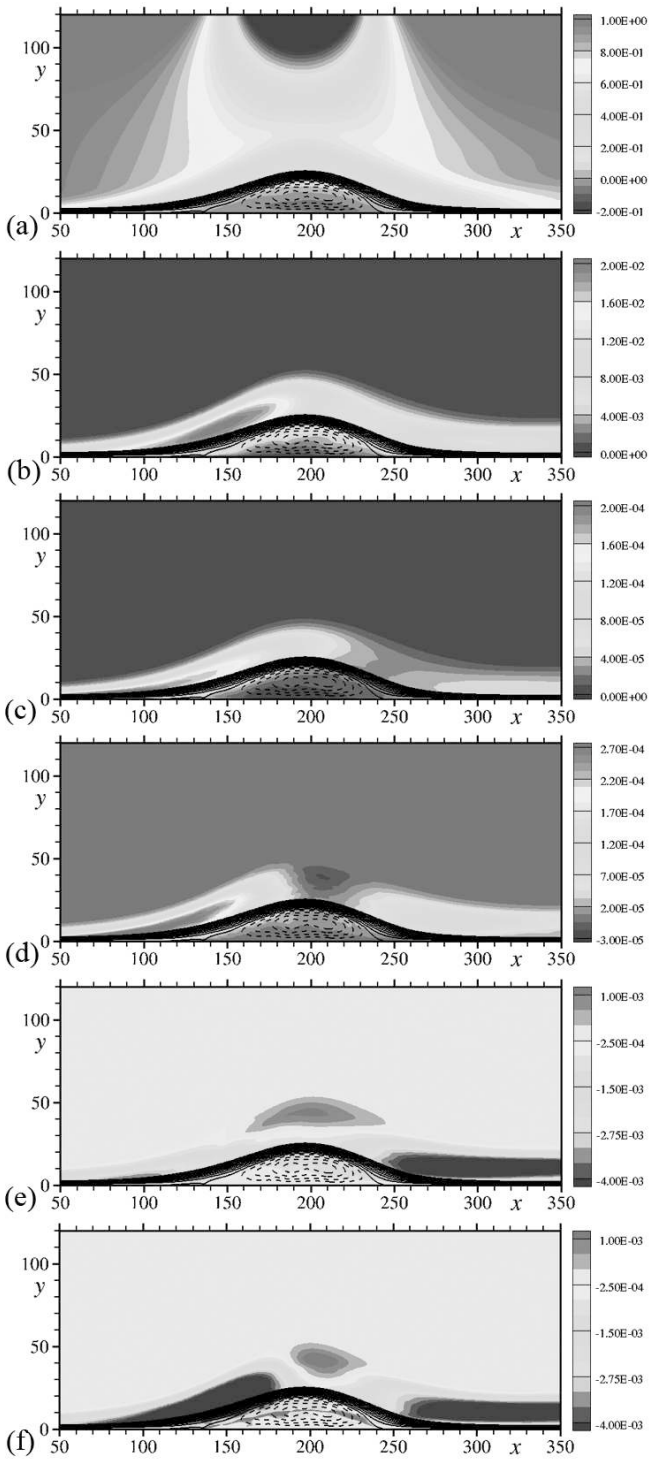

FIGURE 3. Distributions of mean and turbulence statistics for $Re_\theta = 300$: (a) $\bar{U}$; (b) k; (c) ε; (d) P_k; (e) $\overline{u_1 u_2}$; (f) $\overline{ab}$. Solid and dashed lines denote positive and negative streamlines (stream function compared with its wall value).

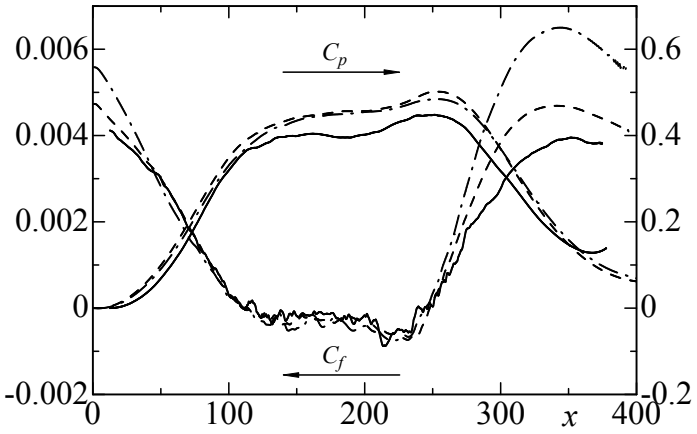

FIGURE 4. Distributions of C_f and C_p: ——, $Re_\theta = 985$; – – –, $Re_\theta = 600$; –·–·–, $Re_\theta = 300$.

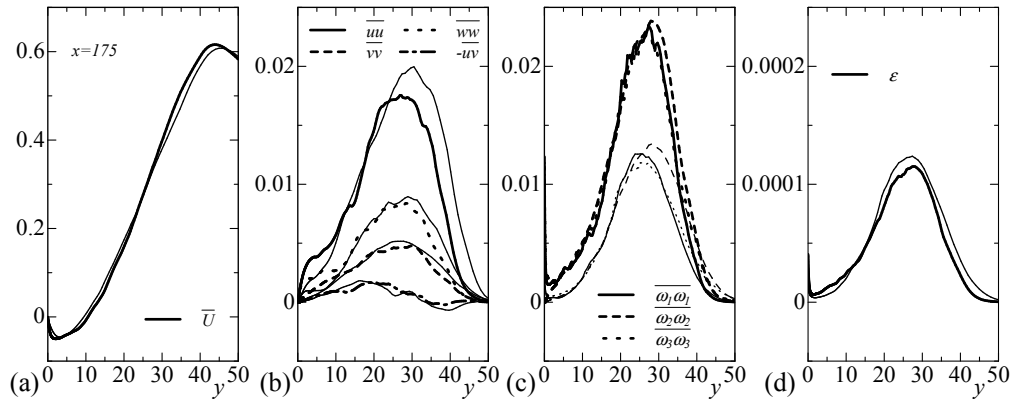

FIGURE 5. Distributions of mean and turbulence statistics in the separated shear layer ($x = 175$): (a) $\bar{U}$; (b) $\overline{u_iu_j}$; (c) $\overline{\omega_i\omega_j}$; (d) ε. Thick and thin lines denote data for $Re_\theta = 600$ and 300, respectively.

3.2. *Reynolds-number dependence*

Now, we focus on the Reynolds-number dependence. Distributions of friction and pressure coefficients, $C_f \left(\equiv 2/U^{+2}_{\infty,0}\right)$ and $C_p \left(\equiv 2\left(P_w - P_{w,0}\right)\right)$, are given in Figure 4 for $Re_\theta =$ 300, 600 and 985 (P_w denotes the wall pressure). In the bubble, we see a decreasing magnitude of C_p with increasing Reynolds number. This is interpreted as an enhanced viscid-inviscid interaction. Also, the rate of decrease of C_f with increasing Re_θ is twice as large in the recovery region as in the inlet region (see $x = 350$ in Figure 4), which may be associated with weak development of near-wall turbulence in the recovery region. It can be expected that this will strongly challenge RANS models.

Another Reynolds-number effect on statistics may be seen in the separated shear layer where the similarity to a mixing layer is sometimes discussed. The Reynolds stresses $\overline{u_iu_j}$, vorticity components $\overline{\omega_i\omega_j}$ and energy dissipation rate ε are shown in Figure 5 together with $\bar{U}$ for $Re_\theta = 300$ and 600 (note that the data for $Re_\theta = 985$ are not shown here

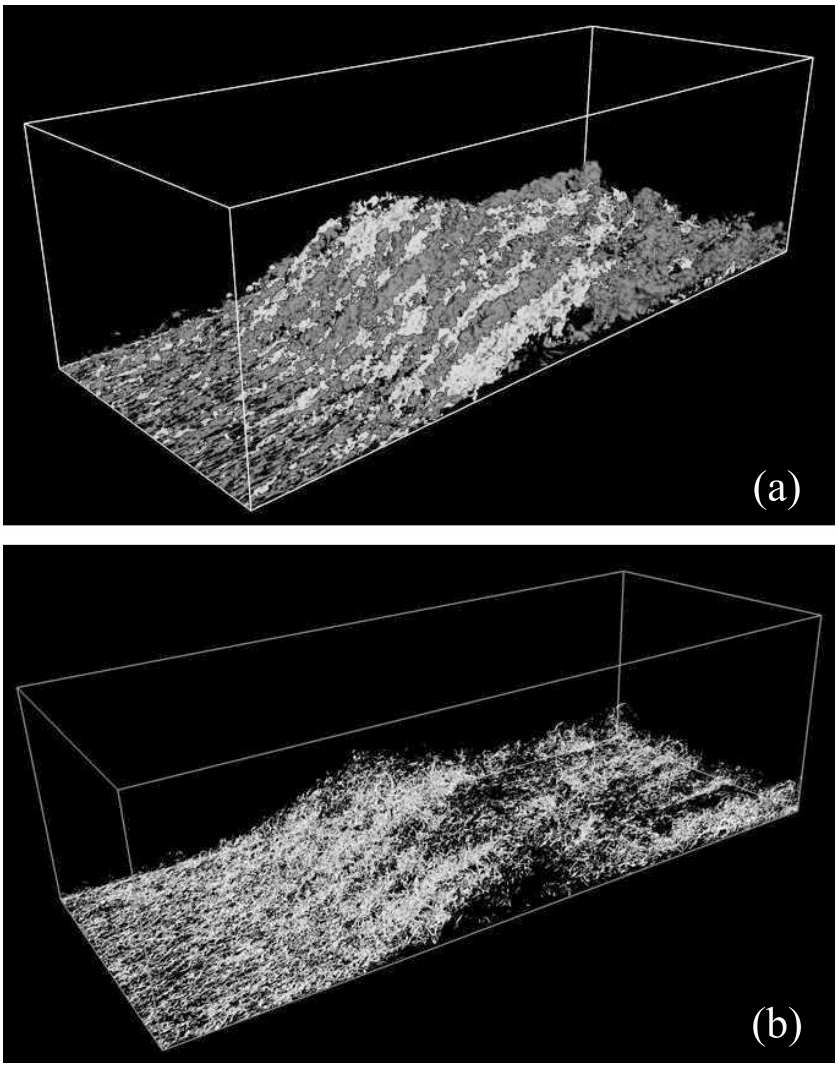

FIGURE 6. Isosurfaces of instantaneous u and Q for $Re_\theta = 985$: (a) Light-gray, $u > 0.15$; dark-gray, $u < -0.15$; (b) white, $Q > 0.01$. The fluid flows from bottom-left to top-right. The visualization domain size shown here is the whole computational domain.

due to insufficient convergence). At this station, the maximum values of $\overline{u_i u_j}$, $\overline{\omega_i \omega_j}$ and ε appear at $y = 25 \sim 30$ where $\bar{U}$ has its maximum gradient and hence inflection point (one exception is $-\overline{u_1 u_2}$ due to the effects of streamline curvature); the Re dependence is very weak; the vorticity component is scaled reasonably after their magnitudes were normalized by the Reynolds number (i.e., a factor of 2 from $Re_\theta = 300$ to 600). This is the classical scaling for free shear flows (Bell & Mehta 1990; Rogers & Moser 1994). Also, the maximum values normalized by the velocity difference ($\Delta U = 0.65$) agree reasonably with those in the mixing layer, viz. $\overline{uu}/\Delta U^2 = 0.042$ (0.025), $\overline{vv}/\Delta U^2 = 0.011$ (0.015), $\overline{ww}/\Delta U^2 = 0.020$ (0.020) (numbers in parentheses are values reported by Rogers &

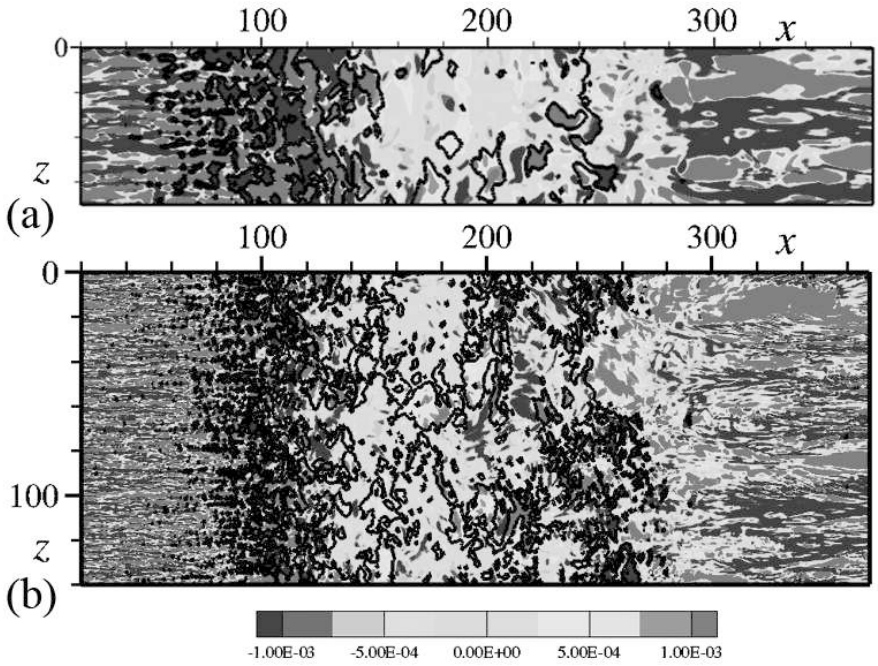

FIGURE 7. Contours of instantaneous τ_1 ($\equiv \mu \partial u/\partial y|_w$) (color) and C_f (line): (a) $Re_\theta = 300$; (b) $Re_\theta = 985$. Lines denote regions of $C_f = 0$.

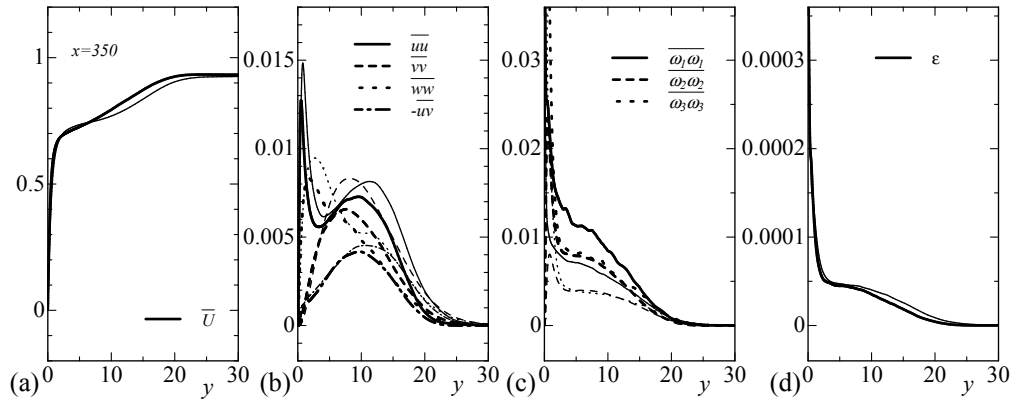

FIGURE 8. Distributions of mean and turbulence statistics in the recovery region ($x = 350$): (a) $\bar{U}$; (b) $\overline{u_i u_j}$; (c) $\overline{\omega_i \omega_j}$; (d) ε. Thick and thin lines denote data for $Re_\theta = 600$ and 300, respectively.

Moser 1994), where a little larger magnitude of $\overline{uu}/\Delta U^2$ may be associated with large-scale organized structures discussed below.

It should however be noted that the classical mixing layer-like structure with large quasi-two-dimensional rollers is not observed in the instantaneous field (see Figure 6 which shows isosurfaces of instantaneous u and $Q(\equiv -u_{i,j}u_{j,i}/2)$ for $Re_\theta = 985$). Instead, there are large-scale positive and negative u structures appearing alternatively in the z direction (Figure 6*a*) at high Re (see also a dense clustering of vortical structures in

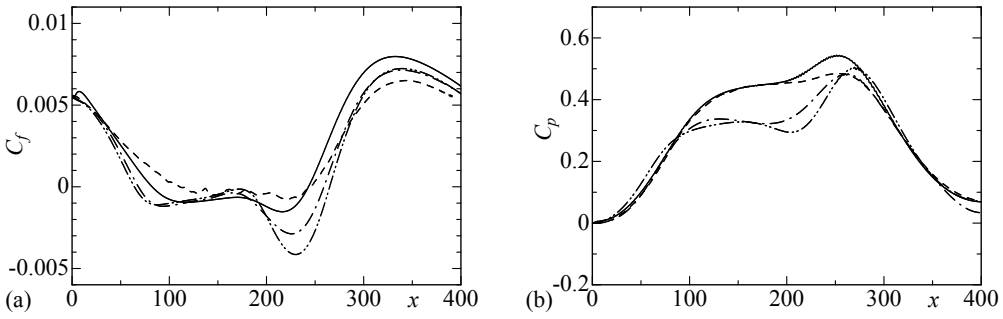

FIGURE 9. Model performance for C_f and C_p at $Re_\theta = 300$: (a) C_f ; (b) C_p. −−−, DNS; ——, k-ε; −·−·−, k-ω; −··−··−, SST.

Figure 6*b*). Also, the u structures are more significant in the reattached region than in the shear layer (Figure 6) probably due to effects of inflectional instabilities originating in the shear layer. The spanwise domain size needs to be large enough to capture the large-scale structures. Indeed, twice the domain adequate for $Re_\theta = 300$ is needed for $Re_\theta = 600$ and 985 to have proper statistics. There are also footprints of large-scale structures onto the wall, i.e., large-scale meandering of the separation lines, large-scale fluctuations in the flow-reversal region, and dense clustering of streaky structures in the reattached region (see Figure 7*b*). The latter clustering is reminiscent of near-wall streaky structures in a turbulent channel flow at higher Reynolds numbers (see, for example, Figure 12 of Abe *et al.* 2004*a* who attributed the clustering to an increasing interaction between the inner and outer region). The apparent streak spacing is, naturally, smaller at the higher Reynolds number after the normalization by θ_0 (Figure 7).

Statistics in the recovery region ($x = 350$) are given in Figure 8, although the present streamwise computational domain is too short to discuss the recovery to a zero-pressure-gradient boundary layer. There are bimodal peaks in the Reynolds stresses (Figure 8*b*): one near the wall and the other in the outer region ($y = 10 \sim 15$). The latter corresponds to the region where $\bar{U}$ has its local maximum gradient. While small-scale quantities ($\overline{\omega_i\omega_j}$ and ε) tend to exhibit mixing layer-like behaviors (Figures 8*c* and *d*), such scaling is no longer applicable for $\overline{u_iu_j}$ (see the significant Re dependence). Also, the magnitude of $-\overline{uv}$ is half as large as those of the normal stresses (three components being nearly the same magnitudes), suggesting intense turbulence state in the outer region. Close inspection revealed that large-scale u structures carry a substantial fraction of the Reynolds shear-stress and hence are active in the transport of streamwise momentum. There is large departure from the logarithmic law established in the zero-pressure-gradient turbulent boundary layer for the $\bar{U}^+$ profile (not shown here).

3.3. *Two-equation model testing*

Finally, we turn our attention to turbulence model testing. Three models, namely k-ε (Abe *et al.* 1994), k-ω (Wilcox 1988) and SST (Menter 1994), are examined (note that the author of the first article is Dr. K. Abe). The inlet data are provided by the DNS data. By this we mean the turbulent kinetic energy k and the eddy viscosity ν_t; we emphasize that we match the inflow eddy viscosity ν_t, rather than the specified dissipation rate (or turbulence frequency) ω for k-ω and SST. Note that in the k-ε model, prescription of ε from k and $\nu_t (\equiv 0.09 f_\mu k^2/\varepsilon)$ is not straightforward due to the presence of near-wall

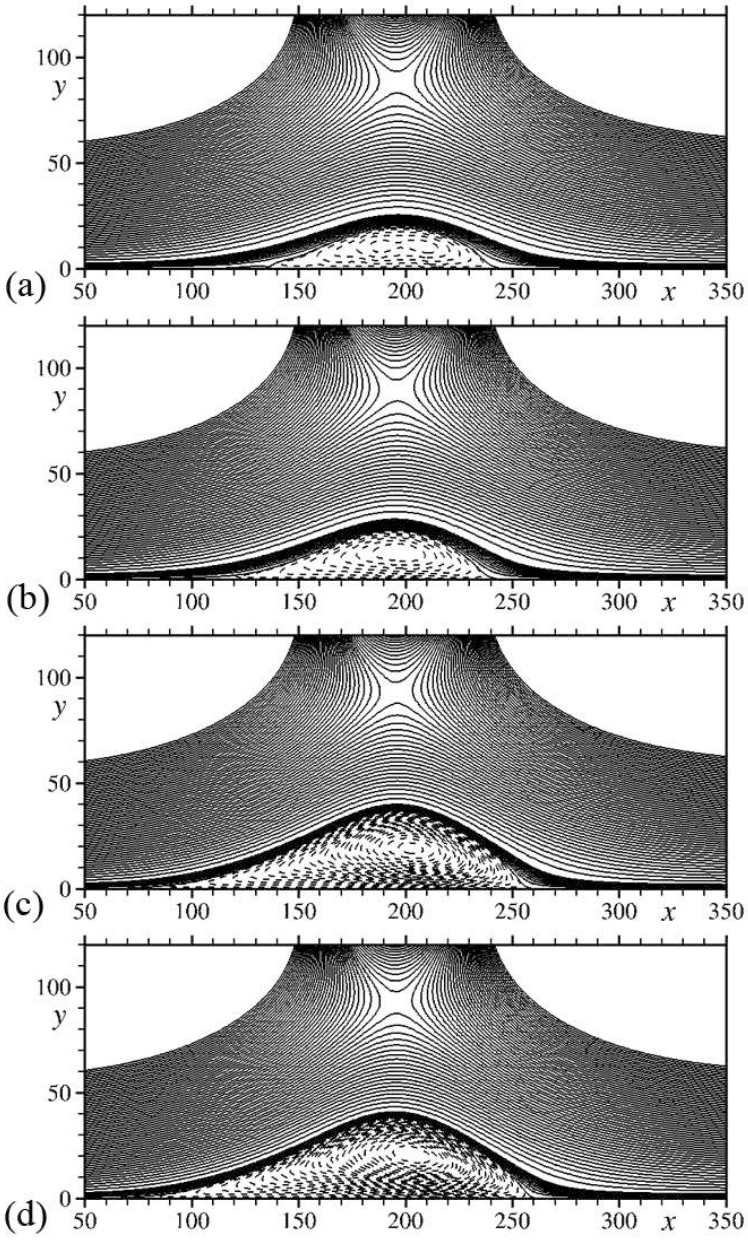

FIGURE 10. Model performance for streamlines at $Re_\theta = 300$: (a) DNS; (b) k-ε; (c) k-ω; (d) SST. Solid and dashed lines denote positive and negative streamlines.

damping function f_μ so that k and ε are used. Indeed, use of k and ν_t as the inflow conditions is effective for having a smooth C_f distribution near the inlet region (see Figure 9*a*). The same grid is used as for DNS, in the (x, y) plane, which allows us to make direct comparisons between DNS and RANS results readily.

Figures 9 to 11 show some representative results on turbulence model testing. Overall, the k-ε model (Abe *et al.* 1994) gives the best prediction among the three models. The

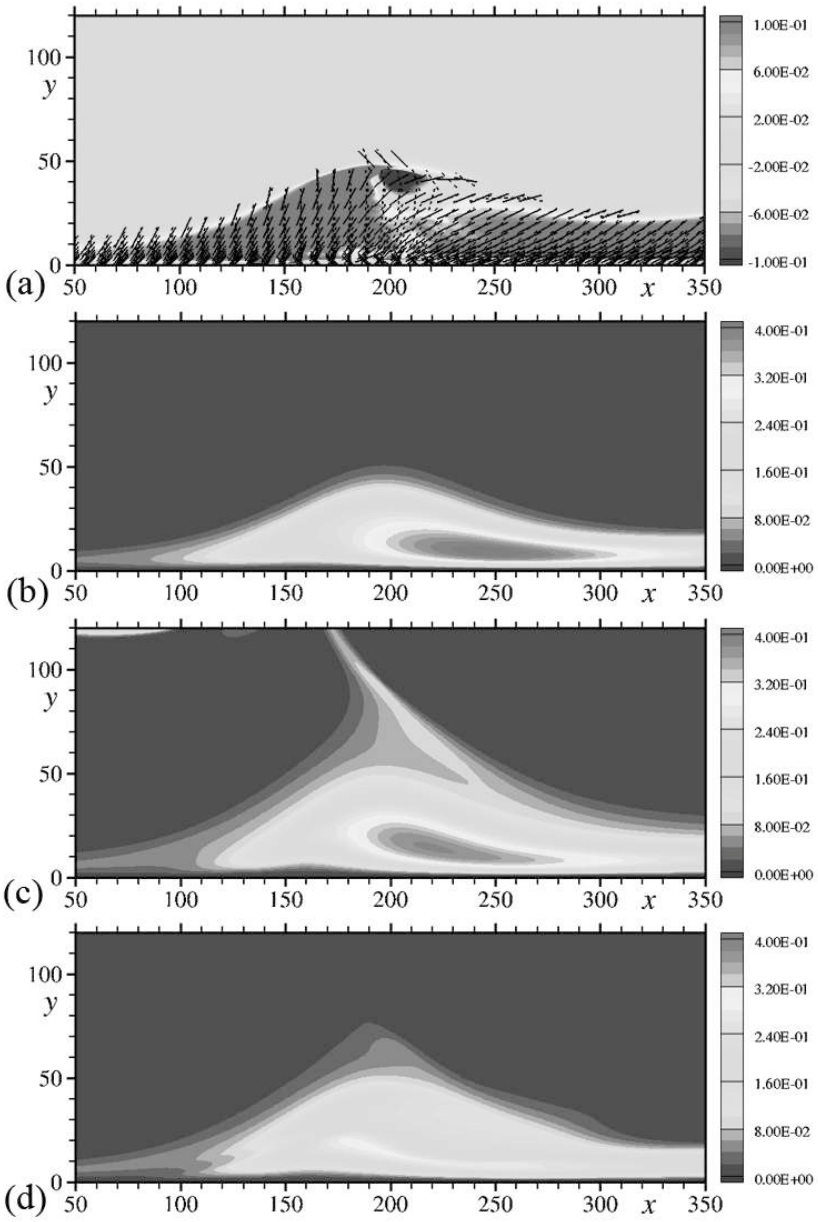

FIGURE 11. Model performance for ν_t at $Re_\theta = 300$: (a) DNS; (b) k-ε; (c) k-ω; (d) SST. In (a), solid and dashed lines denote eigenvectors (associated with the positive eigenvalue) of S_{ij} and $-\overline{u_i u_j}$, respectively. Note the definition in DNS, $\nu_t \equiv -\overline{u_i u_j} S_{ij}/2S_{kl}S_{kl}$, which is a coordinate-invariant form.

present result may not be surprising given that this model predicts the backward facing step reasonably well. The k-ω (Wilcox 1988) and SST (Menter 1994) models tend to show a larger separation bubble than the k-ε model (Figure 10). Note that the prediction improves for the high Re case (the results are not converged enough to be shown here).

One may notice that in the k-ω model a noticeable surge of the turbulent eddy viscosity

ν_t appears close to the upper boundary (Figure 11). This is due to the presence of large velocity gradient close to the upper boundary, which leads to significant disturbances in the k-ω model since the production term for the ω equation is expressed as $\gamma 2S_{ij}^2$ ($\gamma(>0)$ being a model coefficient). The limiter $min(P_k, 10\varepsilon)$ for both k and ω equations in the SST model avoids this disturbance successfully. In this figure, an effective eddy viscosity, $\nu_t \equiv -\overline{u_i u_j} S_{ij}/2S_{kl}S_{kl}$, is proposed from the DNS, which can be described as a least-squares fit to the Reynolds-stress tensor, or as the scalar eddy viscosity which provides the correct production. As a result, it takes negative values in the region of negative P_k (Figures 3*d* and 11*a*); RANS models are certainly not expected to follow such behavior (Figures 11*b–d*). Also, in the negative ν_t region, we see rapid re-orientation of strain eigenvector, while the direction of stress eigenvector changes slowly (see misalignment between the two eigenvectors in Figure 11*a*), which is another interpretation for negative P_k (note that P_k is described as the product of strain and stress tensors, so that P_k becomes negative when their directions are more than 45° different). This approach to exploiting DNS fields is not wide-spread, but appears to have potential. For instance, the eddy viscosity of the models is much smaller than that of the DNS over large areas, but this short separation bubble may be dominated by the inviscid transport of vorticity, so that the velocity does not respond rapidly to inaccuracies in the modeling.

4. Conclusions and future work

In this brief, we have presented some representative DNS results in a turbulent boundary layer with separation and reattachment for inflow $Re_\theta = 300$, 600 and 985. Also reported are results regarding two-equation model testing made using the resulting DNS data. The main conclusions are:

(1) The effects of streamline curvature cannot be dismissed in the separation bubble. In particular, the magnitudes of turbulence quantities are attenuated at the top of the bubble, which can be attributed to the convex curvature, or to the rapid re-orientation of the principal axes of the strain tensor.

(2) The Re effects on statistics are a decreasing magnitude of C_p in the bubble with increasing Re_θ. In the shear layer, free-shear-flow scaling appears to be applicable to a good degree statistically, both for the Reynolds stresses and the dissipation. The same is however not true in the instantaneous field. In addition, the recovery after reattachment has a strong Reynolds-number dependence.

(3) At high Re, there are large-scale organized u structures in the separated and reattached region. There are also their footprints onto the wall, viz., large-scale meandering of the separation lines, large-scale fluctuations in the separated region and dense clustering of streaky structures in the reattached region.

(4) The k-ε model (Abe *et al.* 1994) gives the best prediction among the three models, which is a little unusual; the k-ω (Wilcox 1988) and SST (Menter 1994) models show a larger separation bubble than the k-ε model.

(5) A troublesome freestream sensitivity appears in the k-ω model due to the presence of large velocity gradients combined with stagnation close to the upper boundary. This is a peculiarity of the domain we used, which we may correct in the future. The limiter $min(P_k, 10\varepsilon)$ in the SST model, designed precisely for stagnation regions, avoids this shortcoming successfully.

The present DNS statistics will be open to public access via `http://www.iat.jaxa.jp/db/index.html`.

Acknowledgments

Computations performed on JAXA (Japan Aerospace Exploration Agency) Supercomputer System are gratefully acknowledged. H.A. would like to thank Prof. P. Moin for his hospitality and stimulating discussions during the stay at CTR and also Profs. J. K. Eaton, S. K. Lele and G. Iaccarino for invaluable comments on the present work. Dr. S. Bose reviewed this manuscript.

REFERENCES

Abe, H., Kawamura, H. & Choi, H. 2004*a* Very large-scale structures and their effects on the wall shear-stress fluctuations in a turbulent channel flow up to $Re_\tau = 640$. *ASME J. Fluids Eng.* **126**, 835–843.

Abe, H., Kawamura, H. & Matsuo, Y. 2004*b* Surface heat-flux fluctuations in a turbulent channel flow up to $Re_\tau = 1020$ with Pr=0.025 and 0.71. *Int. J. Heat and Fluid Flow* **25** (3), 404–419.

Abe, K., Kondoh, T. & Nagano, Y. 1994 A new turbulence model for predicting fluid flow and heat transfer in separating and reattaching flows - I. flow field calculations. *Int. J. Heat Mass Transfer* **37** (1), 139–151.

Bell, J. H. & Mehta, R. D. 1990 Development of a two-stream mixing layer from tripped and untripped boundary layers. *AIAA J.* **28** (12), 2034–2042.

Leschziner, M. A. 2006 Modelling turbulent separated flow in the context of aerodynamic applications. *Fluid Dyn. Res.* **38**, 174–210.

Lund, T. S., Wu, X. & Squires, K. D. 1998 Generation of turbulent inflow data for spatially-developing boundary layer simulation. *J. Comput. Phys.* **140** (2), 233–258.

Manhart, M. & Friedrich, R. 2002 DNS of a turbulent boundary layer with separation. *Int. J. Heat and Fluid Flow* **23** (5), 572–581.

Menter, F. R. 1994 Two-equation eddy-viscosity turbulence models for engineering applications. *AIAA J.* **32** (8), 1598–1605.

Morinishi, Y., Lund, T. S., Vasilyev, O. V. & Moin, P. 1998 Fully conservative higher order finite difference schemes for incompressible flow. *J. Comput. Phys.* **143** (1), 90–124.

Na, Y. & Moin, P. 1998 Direct numerical simulation of a separated turbulent boundary layer. *J. Fluid Mech.* **374**, 379–405.

Purtell, L. P., Klebanoff, P. S. & Buckley, F. T. 1981 Turbulent boundary layer at low reynolds number. *Phys. Fluids* **24** (5), 802–811.

Rogers, M. M. & Moser, R. D. 1994 Direct simulation of a self-similar turbulent mixing layer. *Phys. Fluids* **8** (2), 903–923.

Simpson, R. L. 1989 Turbulent boundary-layer separation. *Ann. Rev. Fluid Mech.* **21** (5), 205–234.

Skote, M. & Henningson, D. S. 2002 Direct numerical simulation of a separated turbulent boundary layer. *J. Fluid Mech.* **471**, 107–136.

Song, S. & Eaton, J. K. 2004 Reynolds number effects on a turbulent boundary layer with separation, reattachment, and recovery. *Exp. Fluids* **36**, 246–258.

Spalart, P. R. & Coleman, G. N. 1997 Numerical study of a separation bubble with heat transfer. *Eur. J. Mech. B/Fluids* **16** (2), 169–189.

Wilcox, D. C. 1988 Reassessment of the scale-determining equation for advanced turbulence models. *AIAA J.* **26** (11), 1299–1310.